remote sensing

MDPI

Technical Note

Three-Dimensional Surface Displacements of the 8 January 2022 Mw6.7 Menyuan Earthquake, China from Sentinel-1 and ALOS-2 SAR Observations

Jihong Liu [1], Jun Hu [1,*], Zhiwei Li [1], Zhangfeng Ma [2], Jianwen Shi [1], Wenbin Xu [1] and Qian Sun [3]

[1] School of Geosciences and Info-Physics, Central South University, Changsha 410083, China; liujihong@csu.edu.cn (J.L.); zwli@csu.edu.cn (Z.L.); shijianwen1129@csu.edu.cn (J.S.); wenbin.xu@csu.edu.cn (W.X.)

[2] School of Earth Sciences and Engineering, Hohai University, Nanjing 211100, China; jspcmazhangfeng@hhu.edu.cn

[3] College of Resources and Environmental Science, Hunan Normal University, Changsha 410081, China; sandra@hunnu.edu.cn

* Correspondence: csuhujun@csu.edu.cn

Citation: Liu, J.; Hu, J.; Li, Z.; Ma, Z.; Shi, J.; Xu, W.; Sun, Q. Three-Dimensional Surface Displacements of the 8 January 2022 Mw6.7 Menyuan Earthquake, China from Sentinel-1 and ALOS-2 SAR Observations. *Remote Sens.* **2022**, *14*, 1404. https://doi.org/10.3390/rs14061404

Academic Editor: Francesca Ardizzone

Received: 11 February 2022
Accepted: 9 March 2022
Published: 14 March 2022

Abstract: The 8 January 2022 Mw6.7 Menyuan earthquake was generated in the transition zone between the western Lenglongling fault and the eastern Tuolaishan fault, both being part of the Qilian–Haiyuan fault system with an important role in the adjustment of the regional tectonic regime. In this study, four pairs of SAR (synthetic aperture radar) data from Sentinel-1 and ALOS-2 (Advanced Land Observation Satellite-2) satellites were used to derive the surface displacement observations along the satellite line-of-sight (LOS) and azimuth directions using the differential interferometric SAR (InSAR, DInSAR), pixel offset-tracking (POT), multiple aperture InSAR (MAI), and burst overlap InSAR (BOI) methods. An SM-VCE method (i.e., a method for measuring three-dimensional (3D) surface displacements with InSAR based on a strain model and variance component estimation) was employed to combine these derived SAR displacement observations to calculate the 3D co-seismic displacements. Results indicate that the 2022 Menyuan earthquake was dominated by left-lateral slip, and the maximum horizontal and vertical displacements were 1.9 m and 0.6 m, respectively. The relative horizontal surface displacement across the fault was as large as 2–3 m, and the fault-parallel displacement magnitude was larger on the southern side of the fault compared with the northern side. Furthermore, three co-seismic strain invariants were also investigated, revealing that the near-fault area suffered severe deformation, and two obviously expanding and compressed zones were identified. We provide displacements/strains derived in this study in the prevailing geotiff format, which will be useful for the broad community studying this earthquake; in addition, the SM-VCE code used in this study is open to the public so that readers can better understand the method.

Keywords: the 2022 Menyuan earthquake; three-dimensional displacements; InSAR; SM-VCE

1. Introduction

At 1:45:30 a.m. on 8 January 2022 (local time), an Mw = 6.7 earthquake occurred about 54 km northwest of Menyuan county, Qinghai province, China with a focal depth of about 10 km [1,2]. This earthquake was generated in the transition zone between the western Lenglongling fault (LEF) and the eastern Tuolaishan fault (TF), both being part of the Qilian–Haiyuan fault system (QHFS) (Figure 1). The QHFS comprises from west to east the following structures: the TF, LEF, Jinqianghe fault (JF), Maomaoshan fault (MF), Laohushan fault (LAF), and Hauyuan fault (HF) [3]. This fault system is generally characterized by left-lateral slip and is one of the most important fault systems in the northeastern boundary of the Qinghai–Tibet Plateau block [4]. In this fault system, the northeastward movements of the Qinghai–Tibet Plateau block are resisted by the Gebi–Alashan block and the Huabeikelatong block (see Figure 1), and the tectonic movement direction changes clockwise slowly [5–7]. The left-lateral QHFS can just compensate for these complicated tectonics. Within this fault system, the segment between the LEF, JF, MF, and LAF is considered as a seismic gap and requires more attention [8,9]. Although two Mw > 6.0 events occurred near the LEF (see Figure 1), their fault slip mechanisms were obviously inconsistent with the overall left-lateral slip of the QHFS [5]. Investigations show that these two events may have been related to the northern Lenglongling fault (NLEF), which is an associated thrust fault located in the northern part of the western LEF [5,10]. According to the field investigation and geodesy observations [2,11], this 2022 Menyuan earthquake was a typical left-lateral seismic event, which is consistent with the overall pattern of the QHFS. Therefore, it is significant to swiftly obtain the ground surface displacement of this earthquake, thus providing reliable observations for the fault mechanism analysis and the overall seismic risk assessment of the QHFS.

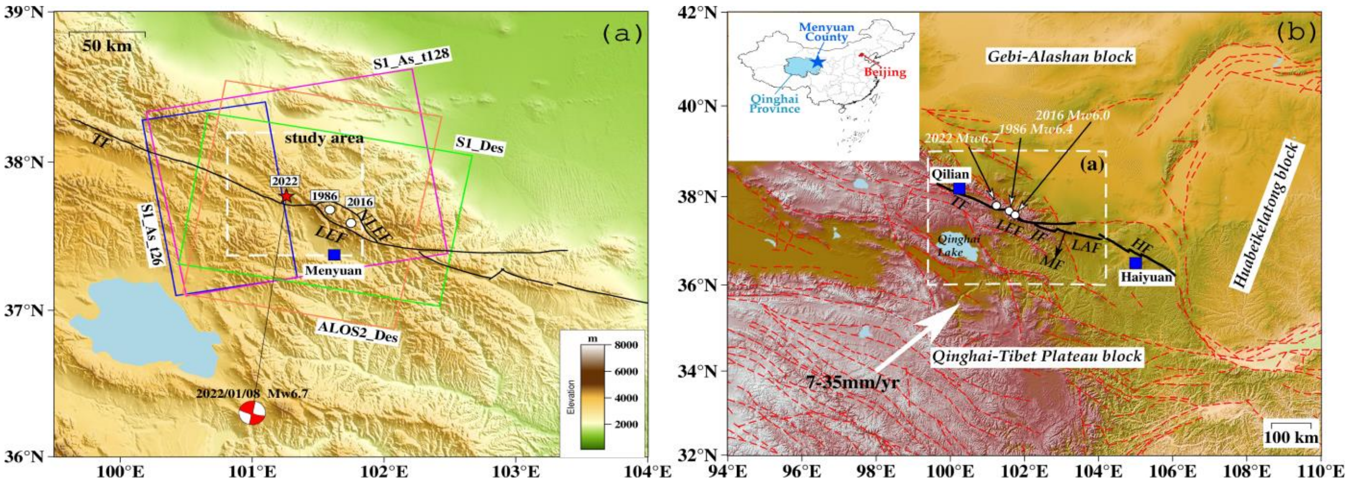

Figure 1. (**a**) Color-shaded relief map. The solid rectangles represent the footprint of the used SAR data. The white dashed rectangle outlines the study area (i.e., the range of Figures 2–5). The black lines are the location of mapped faults. The red beach ball and the red star are the focal mechanism and the epicenter of the 2022 Menyuan earthquake, respectively. White circles are two historic Mw > 6.0 earthquakes near the Lenglongling Fault (LEF) and the northern LEF (NLEF) that occurred in 1986 and 2016. The blue square is Menyuan county. (**b**) The tectonic setting around the study area. The red dashed lines are the mapped faults. The bold black lines are the QHFS with the Tuolaishan fault (TF), LEF, Jinqianghe fault (JF), Maomaoshan fault (MF), Laohushan fault (LAF), and Hauyuan fault (HF). The white dashed rectangle indicates the range of (**a**). The insert map shows the location of Menyuan county (the blue star) in China. The white arrow denotes the northeastward movement (about 7–35 mm/year) of the Qinghai–Tibet Plateau block [6,7]. Blue squares are Qilian county and Haiyuan county.

Benefiting from the open Sentinel-1 synthetic aperture radar (SAR) data with regular acquisitions, scientists soon obtained the ascending/descending Sentinel-1 SAR image pairs on 10 January 2022, 2 days after the earthquake, providing a data basis for revealing the surface displacement of this earthquake. In particular, Li et al. [2] quickly obtained the co-seismic displacements along the satellite line-of-sight (LOS) direction from the ascending/descending Sentinel-1 SAR images using the differential interferometric SAR (InSAR, DInSAR) method, and then investigated the source parameters and slip distributions of the 2016 and 2022 Menyuan earthquakes. Moreover, Yang et al. [11] used the same SAR data and displacement observations to construct a finite fault model of this event, indicating that multiple fault segments ruptured during this earthquake. However, the used ascending SAR image pair only covers part of the deforming zone and cannot reflect the complete deformation pattern of this earthquake. Furthermore, since the DInSAR LOS displacements can only capture the one-dimensional projection of the real three-dimensional (3D) displacements, ascending/descending DInSAR LOS displacements cannot directly reveal the real deformation characteristics and cannot adequately constrain the fault slip model.

After several days of the earthquake, multiple SAR data with complete coverage (e.g., advanced land observation satellite-2, ALOS-2, and Sentinel-1) were available; therefore, it is feasible to obtain different SAR observations with various imaging geometries using various data processing methods (e.g., DInSAR [12], pixel offset-tracking, POT [13], multiple aperture InSAR, MAI [14], and burst overlap InSAR, BOI [15]), as well as to calculate the 3D displacements of this earthquake. For calculating 3D displacements, the traditional weighted least square (WLS) method (e.g., [16,17]) calculates 3D displacements of a target point using only the SAR observations at this point, and it determines the variances/weights of SAR observations on the basis of some *a priori* information, e.g., the displacements within a limited range are constant. However, the real deformations at adjacent points are generally correlated under the action of continuous stress, and the *a priori* information cannot adequately reflect the real complex noise distributions of SAR observations. Therefore, the WLS-obtained 3D displacements generally have a lower accuracy. Compared with the WLS method, a method for measuring 3D surface displacements with InSAR based on a strain model (SM) and variance component estimation (VCE) (SM-VCE method) [18], which was developed by our team, has proven to be superior in estimating 3D displacements [19–21]. The superiority lies in the fact that (1) the SM is applied to describe the correlation of 3D displacements between adjacent points and to establish the relationship between the 3D displacements at a target point and SAR observations at surrounding points, and (2) the well-known VCE algorithm is used to accurately determine the weights of SAR observations in an a posteriori manner.

In this study, we focus on estimating a complete and accurate 3D co-seismic displacement field related to the 2022 Menyuan earthquake on the basis of the ascending/descending Sentinel-1 SAR data and descending ALOS-2 SAR data. The DInSAR, POT, MAI, and BOI [15] methods are all used to measure the ground surface displacements along the line-of-sight (LOS) or azimuth directions. The SM-VCE method was applied here to combine the DInSAR-, MAI-, POT-, and BOI-derived displacement observations to obtain 3D co-seismic displacements of the 2022 Menyuan earthquake. Since more SAR displacement observations are used and an advanced method (i.e., SM-VCE) is applied to calculate 3D displacements, the obtained 3D displacements can accurately reveal the co-seismic deformation of this earthquake and provide a reliable dataset for further model interpretation. Moreover, the co-seismic strains were also calculated on the basis of the 3D displacements. In particularly, to benefit more researchers interested in co-seismic surface deformation assessment and the SM-VCE method, the obtained displacement data in geotiff format and the used SM-VCE code can be freely downloaded (see Data Availability Statement).

2. Data and Methods

2.1. The Used SAR Data

Table 1 presents the basic information of the SAR data used in this paper. Their coverages can be found in Figure 1. All of these SAR data were acquired at several days after the earthquake; therefore, it is inevitable to include the post-seismic deformations in the SAR-derived displacement observations, which is normal for SAR earthquake studies [22,23]. We also investigated the post-seismic displacement in the descending Sentinel-1 pair 20220110–20220122, and we found that the post-seismic displacement of this earthquake was negligible compared with the co-seismic displacement; therefore, it was practical to combine these SAR-data-derived observations to obtain a 3D displacement field even though the SAR acquisition dates were inconsistent.

The DInSAR, POT, MAI, and/or BOI methods were applied here to obtain the displacement observations from the aforementioned SAR data, and the details of the data processing procedure can be found in [21]. As for the ALOS-2 MAI displacement observation, we conducted a directional filtering and interpolation procedure to mitigate the possible ionospheric noise [24]. Figure 2 shows the SAR displacement observations. As can be seen, the spatial patterns of the SAR displacements with similar imaging geometry were consistent with each other, e.g., the LOS displacements from DInSAR and POT method (i.e., the first and second columns in Figure 2). Nevertheless, different method-derived displacements have their own superiorities. For example, the DInSAR LOS displacement has a much higher accuracy compared with the POT LOS displacement, but the POT method can measure larger displacement gradient compared with the DInSAR method. Although the POT/MAI/BOI methods have a lower displacement accuracy, they can obtain the displacements along the azimuth direction (near the north–south direction), which is significant since the DInSAR LOS displacement is almost blind to the north–south displacement component. Since the accuracy of the POT method depends highly on the spatial resolution of the used SAR images, the POT-derived azimuth displacements of Sentinel-1 data and the LOS displacements of ALOS-2 data were seriously contaminated by noise. Hence, these four SAR displacement observations (i.e., Figure 2c,g,k,n) were not used to calculate the 3D co-seismic displacements of this earthquake.

Table 1. Basic information of the SAR data used in this paper.

Sensor	Orbit Direction	Master-Slave Date	Track	Spatial Perpendicular Baseline (m)	Wavelength (cm)	Incident Angle (°)	Azimuth Angle (°)	Pixel Resolution (m) (Range × Azimuth)	Imaging Mode
Sentinel-1	Ascending	20211229–20220110	T26	−104	5.6	44	−13	2.3 × 14.0	TOPS
Sentinel-1	Ascending	20220105–20220117	T128	39	5.6	37	−13	2.3 × 14.0	TOPS
Sentinel-1	Descending	20211229–20220110	T33	56	5.6	37	−167	2.3 × 14.0	TOPS
ALOS-2	Descending	20201212–20220123	T41	296	23.6	34	−167	8.6 × 2.1	ScanSAR

2.2. The SM-VCE Method

To obtain the 3D co-seismic displacements of the 2022 Menyuan earthquake, the SM-VCE method [18] was employed to combine the SAR displacement observations. Compared with the traditional WLS method (e.g., [16,17]) that calculates the 3D displacements for a target point using only the SAR observations at this point, the SM-VCE method incorporates more observations at the surrounding points for calculating the target 3D displacements. This increment relies on the fact that the strain model [25,26] represents the geophysical relationship between 3D displacements of adjacent points and can be used to link the SAR displacement observations at surrounding points with the target 3D displacements.

For example, when calculating the 3D displacements $\boldsymbol{d}^0 = \begin{bmatrix} d_e^0 & d_n^0 & d_v^0 \end{bmatrix}^T$ for point P^0 (the 3D position components are $\boldsymbol{x}^0 = \begin{bmatrix} x_e^0 & x_n^0 & x_v^0 \end{bmatrix}^T$) using the SM-VCE method, it is necessary to predefine a window around P^0. According to the strain model, for a point P^k with 3D position and displacement components being $\boldsymbol{x}^k = \begin{bmatrix} x_e^k & x_n^k & x_v^k \end{bmatrix}^T$ and $\boldsymbol{d}^k = \begin{bmatrix} d_e^k & d_n^k & d_v^k \end{bmatrix}^T$, respectively, we can obtain the following relationship [26]:

$$\boldsymbol{d}^k = \boldsymbol{H} \cdot \Delta^k + \boldsymbol{d}^0, \tag{1}$$

where $\Delta^k = \boldsymbol{x}^k - \boldsymbol{x}^0 = \begin{bmatrix} \Delta x_e^k & \Delta x_n^k & \Delta x_v^k \end{bmatrix}^T$, superscripts e, n, v denote east–west, north–south, and vertical components, respectively, and $\boldsymbol{H}$ is the displacement gradient matrix, which can be written as

$$\boldsymbol{H} = \frac{\partial d}{\partial x} = \begin{bmatrix} \partial d_e / \partial x_e & \partial d_e / \partial x_n & \partial d_e / \partial x_v \\ \partial d_n / \partial x_e & \partial d_n / \partial x_n & \partial d_n / \partial x_v \\ \partial d_u / \partial x_e & \partial d_u / \partial x_n & \partial d_u / \partial x_v \end{bmatrix}. \tag{2}$$

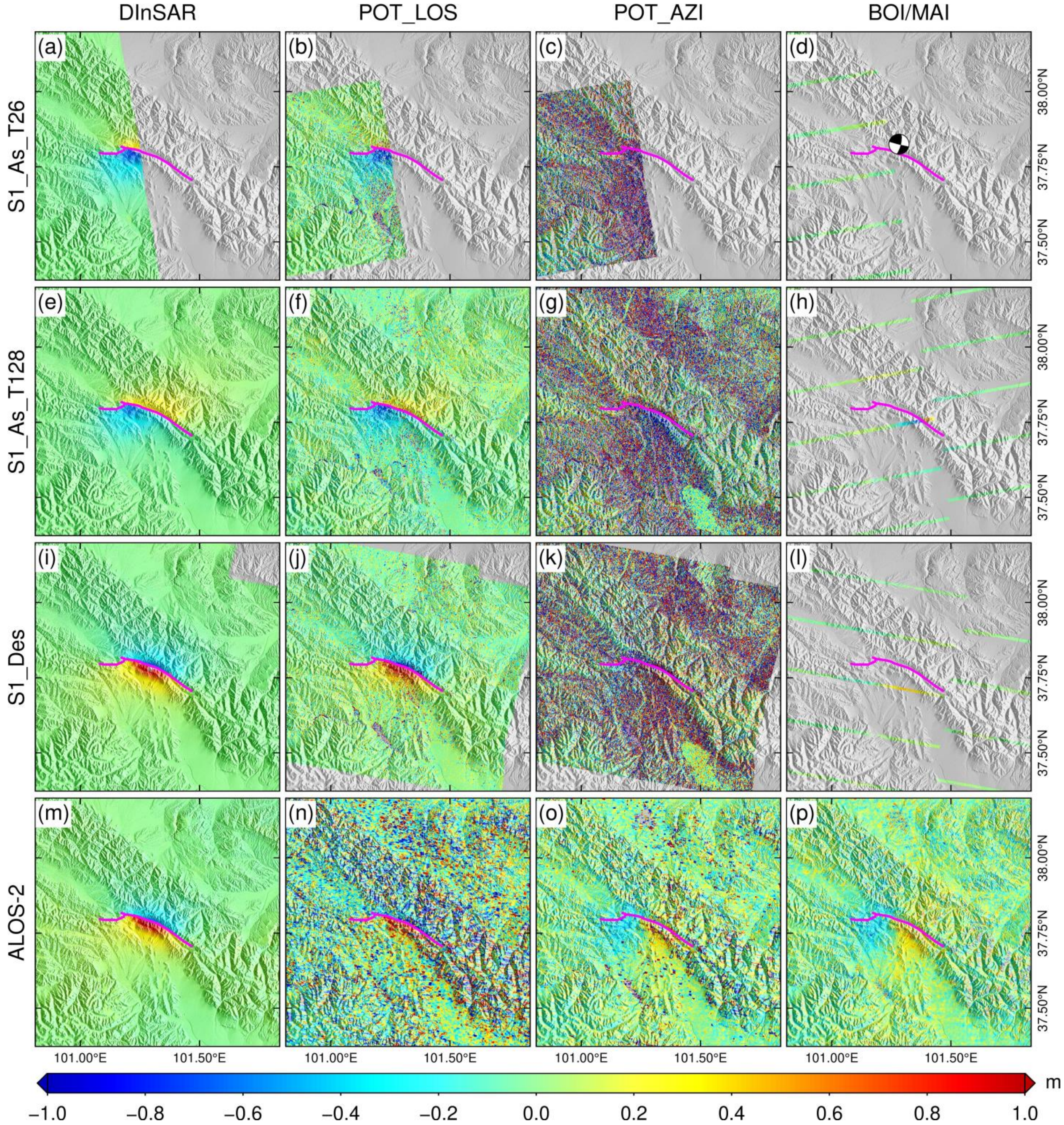

Figure 2. SAR displacement observations from the Sentinel-1 and ALOS-2 data. The magenta lines show the location of the ruptured fault trace, and the beach ball represents the focal mechanism and the epicenter location from the United States Geological Survey (USGS). For a better presentation of the complete displacement pattern, the beach ball is only drawn in (**d**). (**a**–**d**) are SAR observations from ascending Sentinel-1 data of track 26, (**e**–**h**) are from ascending Sentinel-1 data of track 128, (**i**–**l**) are from descending Sentinel-1 data, and (**m**–**p**) are from descending ALOS-2 data.

Generally, $\boldsymbol{H}$ is assumed to be constant in the predefined window. Equation (1) can be rewritten as

$$\boldsymbol{d}^k = \boldsymbol{B}_{\text{sm}}^k \cdot \boldsymbol{l}, \tag{3}$$

$$\boldsymbol{B}_{\mathrm{sm}}^{k}=\begin{bmatrix}1&0&0&\Delta x_{e}^{k}&\Delta x_{n}^{k}&\Delta x_{v}^{k}&0&0&0&0&0&0\\0&1&0&0&0&0&\Delta x_{e}^{k}&\Delta x_{n}^{k}&\Delta x_{v}^{k}&0&0&0\\0&0&1&0&0&0&0&0&0&\Delta x_{e}^{k}&\Delta x_{n}^{k}&\Delta x_{v}^{k}\end{bmatrix}, \quad (4)$$

$$\boldsymbol{l}=\begin{bmatrix}d_{e}^{0}&d_{n}^{0}&d_{v}^{0}&\frac{\partial d_{e}}{\partial x_{e}}&\frac{\partial d_{e}}{\partial x_{n}}&\frac{\partial d_{e}}{\partial x_{v}}&\frac{\partial d_{n}}{\partial x_{e}}&\frac{\partial d_{n}}{\partial x_{n}}&\frac{\partial d_{n}}{\partial x_{v}}&\frac{\partial d_{v}}{\partial x_{e}}&\frac{\partial d_{v}}{\partial x_{n}}&\frac{\partial d_{v}}{\partial x_{u}}\end{bmatrix}^{\boldsymbol{T}}. \quad (5)$$

Assuming that there are J types of SAR displacement observations at P^k, i.e., $\boldsymbol{L}^k=\left[L_1^k,\ L_2^k,\ldots,L_j^k,\ldots,L_J^k\right]^T$ $(j=1,\ 2,\ \ldots,J-1,\ J)$, it is easy to establish the relationship between the 3D displacement components $\boldsymbol{d}^k$ and the observation vector $\boldsymbol{L}^k$.

$$\boldsymbol{L}^k=\boldsymbol{B}_{\mathrm{geo}}^k\cdot\boldsymbol{d}^k, \quad (6)$$

$$\boldsymbol{B}_{\mathrm{geo}}^{k}=\left[\left(\boldsymbol{B}_{\mathrm{geo},1}^{k}\right)^{T},\left(\boldsymbol{B}_{\mathrm{geo},2}^{k}\right)^{T},\ldots,\left(\boldsymbol{B}_{\mathrm{geo},j}^{k}\right)^{T},\ldots,\left(\boldsymbol{B}_{\mathrm{geo},J}^{k}\right)^{T}\right]^{T}, \quad (7)$$

where $\boldsymbol{B}_{\mathrm{geo},j}^k=\begin{bmatrix}a_j^k&b_j^k&c_j^k\end{bmatrix}$ is a unit vector that projects the 3D displacements at point P^k to the corresponding j-th observations, and

$$\begin{cases}a_j^k=-\mathrm{flag}\cdot\sin\left(\theta_j^k\right)\cdot\cos\left(\alpha_j^k\right)\\ b_j^k=\mathrm{flag}\cdot\sin\left(\theta_j^k\right)\cdot\sin\left(\alpha_j^k\right)\\ c_j^k=\cos\left(\theta_j^k\right)\\ \mathrm{flag}=\begin{cases}-1,\ \mathrm{left-looking\ mode}\\ 1,\ \mathrm{right-looking\ mode}\end{cases}\end{cases} \text{ or } \begin{cases}a_j^k=\sin\left(\alpha_j^k\right)\\ b_j^k=\cos\left(\alpha_j^k\right)\\ c_j^k=0\end{cases}, \quad (8)$$

when the L_j^k is the displacement observation along the LOS or AZI direction, respectively. α_j^k and θ_j^k are the satellite heading angle (clockwise from the north) and the radar incidence angle at P^k, respectively [18]. By combining Equations (3) and (6), we can establish the relationship between the unknown vector $\boldsymbol{l}$ and the SAR observations $\boldsymbol{L}^k$.

$$\boldsymbol{L}^k=\boldsymbol{B}^k\cdot\boldsymbol{l}, \quad (9)$$

$$\boldsymbol{B}^k=\boldsymbol{B}_{\mathrm{geo}}^k\cdot\boldsymbol{B}_{\mathrm{sm}}^k. \quad (10)$$

For K_j surrounding points of P^0 for the j-th type of observation, the overall observation functions can be constructed on the basis of Equation (9).

$$\boldsymbol{L}=\boldsymbol{B}\cdot\boldsymbol{l}, \quad (11)$$

$$\boldsymbol{L}=\left[(\boldsymbol{L}_1)^T,\ (\boldsymbol{L}_2)^T\ldots(\boldsymbol{L}_J)^T\right]^T, \quad (12)$$

$$\boldsymbol{B}=\left[(\boldsymbol{B}_1)^T,\ (\boldsymbol{B}_2)^T\ldots(\boldsymbol{B}_J)^T\right]^T, \quad (13)$$

where the size of observation vector $\boldsymbol{L}$ and the coefficient matrix $\boldsymbol{B}$ are $\sum_1^J K_j\times 1$ and $\sum_1^J K_j\times 12$, respectively.

Benefiting from the increasing SAR displacement observations used for calculating the target 3D displacements (i.e., Equation (12)), the famous VCE algorithm [27,28] is used to determine the accurate weights of these J types of SAR displacement observations in a posteriori way.

In the SM-VCE method, one critical parameter is the window size when establishing Equation (11) according to the strain model. Since the displacement gradients are assumed to be constant in the predefined window, too large a window size will violate this assumption, and too small a window size will significantly decrease the number of SAR displacement observations (i.e., K_j), as well as the performance of the VCE algorithm.

In this paper, we empirically determined a window size of 40 pixels × 40 pixels, which corresponds to about 2 km × 2 km with the observations' spatial resolution of about 50 m × 50 m. In such a spatial scale of this case study, the displacement gradients can be regarded as constants, and the spatially high-frequency noises in POT observations can also be well suppressed [21].

3. Results

Figure 3 shows the 3D co-seismic displacements of the Menyuan earthquake derived using the SM-VCE method as a function of the SAR displacement observations in Figure 2. It is easy to infer that this earthquake was dominated by left-lateral strike slip, which is consistent with the overall tectonic movement of the QHFS. The maximum vertical displacement occurred near the ruptured faults with the magnitude of 0.6 m. Since the direction of the ruptured faults was nearly east–west, the east–west displacement component showed much larger magnitude compared with the north–south and vertical components. Figure 3e is the projection of the horizontal displacements to the fault orientation (about 114° clockwise from the north), where the negative and positive values represent northwestward and southeastward horizontal displacements, respectively. The spatial patterns of horizontal displacements on both sides of the fault are generally symmetrical. Figure 3f presents the across-fault displacements of six selected profiles along the fault, illuminating that the maximum horizontal displacement could reach about 1.9 m, and the relative horizontal displacement across both sides of the fault was as large as 2–3 m, which is consistent with the field investigations [11]. In addition, Figure 3f indicates that the absolute displacement magnitude was larger on the southern side of the fault compared with the displacement magnitude on the northern side. This may be attributed to the fact that, across the QHFS, the Qinghai–Tibet Plateau block on the southern side of this fault system is relatively active and continuously pushing northward, but being resisted by the Gebi–Alashan block and the Huabeikelatong block, which are relatively stable compared with the Qinghai–Tibet Plateau block [4,6,29]. In this case, this earthquake is of great significance for studying the tectonic stress across the QHFS.

Figure 4 presents the corresponding variance of the 3D co-seismic displacements estimated using the SM-VCE method. The variances of the east–west and vertical components were generally at a centimeter to millimeter level, while the north–south component was at a decimeter level, which is reasonable since the north–south component was mainly contributed by the low-accuracy SAR azimuth displacements, while the relatively high-accuracy SAR displacements mainly contributed to the east–west and vertical components. In the north–south variance map, there were obvious striped zones with relatively lower values since, at these zones, the BOI observations were also used to calculate 3D displacements. Since the correlation between the north–south and vertical components was high when calculating 3D displacements with the current SAR observations [30], the striped zones also appeared in the vertical variance map. Moreover, a far-field zone (the red dashed rectangles in Figure 3a–c) was selected to assess the accuracy of the obtained 3D displacements. In this zone, we assumed that no co-seismic displacement occurred; hence, the obtained displacement signals in this zone were regarded as noise and could be used to estimate the variance of the corresponding component. The results show that the variance values were 8.6 mm, 27.5 mm, and 5.9 mm for the east–west, north–south, and vertical components, respectively, which are generally consistent with the results in Figure 4.

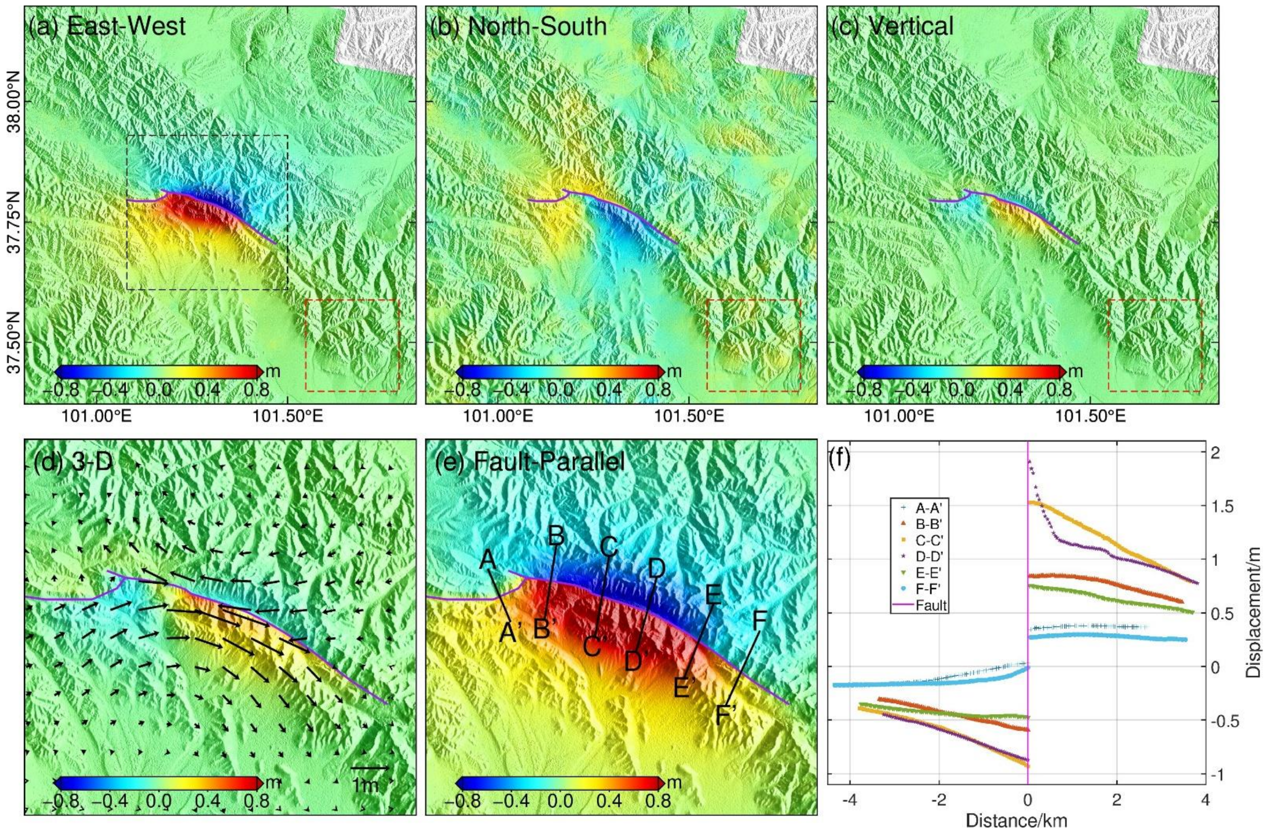

Figure 3. Three-dimensional co-seismic displacements of the 2022 Menyuan earthquake derived using the SM-VCE method. The black dashed rectangle in (**a**) is the range of (**d**,**e**). The red dashed rectangles in (**a**–**c**) are the areas for estimating the variance of the corresponding displacement component. The base map in (**d**) is the vertical displacement, and the arrows are the down-sampled horizontal displacements. (**e**) Fault-parallel horizontal displacements, where the negative and positive values represent northwestward and southeastward horizontal displacements, respectively, and the black lines are the selected profiles across the fault, i.e., profiles A-A′, B-B′, C-C′, D-D′, E-E′, and F-F′. (**f**) The absolute fault-parallel horizontal displacements across the fault.

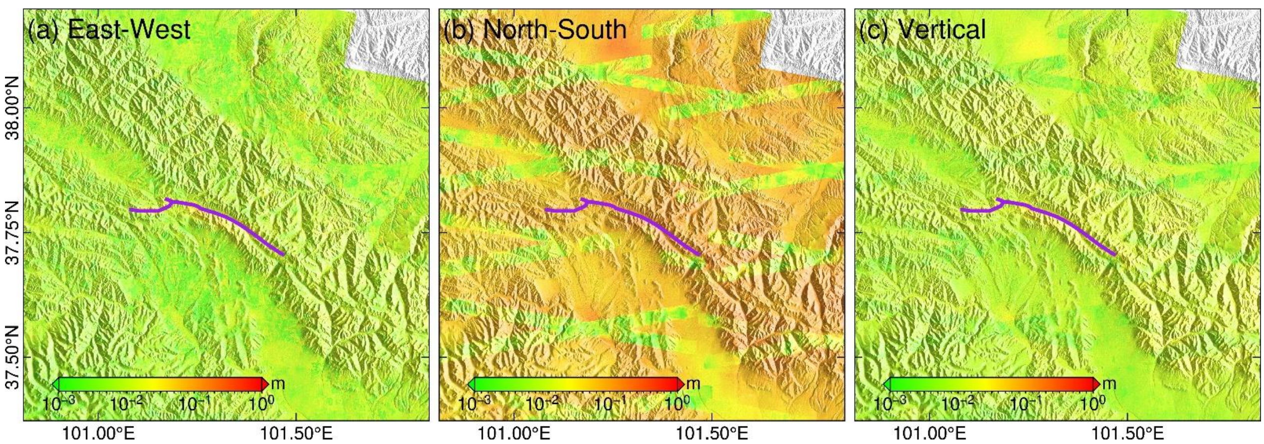

Figure 4. The variance of the 3D co-seismic displacements estimated using the SM-VCE method. (**a**–**c**) are the variance maps for the east-west, north-south, and vertical displacement components, respectively.

4. Discussion

4.1. Three Strain Invariants of the 2022 Menyuan Earthquake

The three strain invariants [21] comprise dilatation, differential rotation, and maximum shear, which are calculated from the 3D displacement gradients, and are independent of any shift and rotation of the coordinate systems [25]. Compared with the displacement fields, the strain fields can provide some unique view about the surface deformations, and they have been widely used for analyzing the inter-seismic deformations on the basis of sparse GNSS (global navigation satellite system) data [31–33]. For example, with respect to the inter-seismic deformations, zones with higher magnitude of the strain invariants indicate a greater potential for stress accumulation and seismic risk [33]. For the high-spatial-resolution co-seismic displacements, it is also practical to calculate the strain invariants and to assist the analysis of co-seismic behavior [34–37] (details about the calculation can be found in [21]). One point that should be noted is that, for the inter-seismic deformations, the deformations are generally continuously occurring; thus, the strain analysis can benefit the assessment of seismic risk. However, for the co-seismic events, since the displacements have occurred, the strain analysis can be used for the disaster assessment and even some post-event analysis.

As shown in Figure 5, the strain invariants were more obvious near the ruptured fault zones compared with the far-field area. This is reasonable since the strains were calculated on the basis of displacement gradients, which were of high magnitude near the fault compared with the far-field area. For the dilatation invariant, the positive and negative values indicate that the volume around this point was expanding and compressed, respectively. As shown in Figure 5a, there were two obvious positive (expanding) zones and two obvious negative (compressed) zones near the fault. By comparing with the horizontal displacements (Figure 3d), it can be found that the expanding or compressed zones corresponded to the areas with increasing or decreasing magnitude of horizontal displacements, respectively. Both the expanding and the compressed areas can be considered to be deformed due to the external force. This force may not only be related to the inter-seismic deformation but also affect the post-event behavior of the fault, and further investigations can be conducted with respect to the dilatation invariant. For the differential rotation invariant, negative or positive values represent the clockwise or anticlockwise rotation of the horizontal displacements around a target point. It is easy to infer that both sides of the fault experienced a similar clockwise rotation, which is consistent with the horizontal displacement pattern, whereby the horizontal displacement direction changed gradually to the right of the current direction (Figure 3d). For the maximum shear invariant, the value was positive, generated in the area where relative horizontal displacements occurred. For example, given two points with a similar horizontal direction, but with different magnitudes, there will be maximum shear strain. As can be seen, the maximum shear strain signal only concentrated near the fault area, indicating that significant relative deformations occurred in these zones.

4.2. The Contributions of Different SAR Observations to the 3D Displacements

It is necessary to combine SAR displacement observations from at least three imaging geometries with significant difference for calculating the real 3D displacements. For the current SAR satellites, two imaging geometries can be easily obtained, i.e., ascending and descending DInSAR LOS directions with the right-looking mode. The LOS observations are sensitive to the east–west and vertical displacement components, but almost blind to the north–south component. Therefore, by combing the easily acquired ascending/descending DInSAR LOS observations, many studies and applications have been conducted to only estimate the east–west and vertical displacements by ignoring the north–south component [30,38–42]. In order to obtain the real 3D displacements, one must find at least one another SAR displacement observation that can complement the ascending/descending DInSAR LOS observations. Considering the current SAR data and the data processing methods, there are mainly two ways to realize the calculation of 3D displacements. One way is to incorporate the left-looking mode SAR data, whose imaging geometry is quite different from the right-looking mode SAR data. By combining ascending/descending left-/right-looking mode SAR data, it is practical to calculate 3D displacements with high accuracy using only the DInSAR method [19,43]. The main shortcoming lies in that left-looking SAR data are rarely available. Another way is to incorporate the azimuth SAR displacement observations. In addition to the DInSAR method, the POT, MAI, and BOI methods can derive the displacement observations along the satellite azimuth direction, which is near the north–south direction. In this case, by combining the ascending/descending SAR data with the DInSAR and POT/MAI/BOI methods, it is also feasible to calculate reliable 3D displacements [44–50]. Since the accuracy of POT/MAI/BOI methods is not as high as that of the DInSAR method, the measurable north–south displacement magnitude is generally higher than a dozen centimeters.

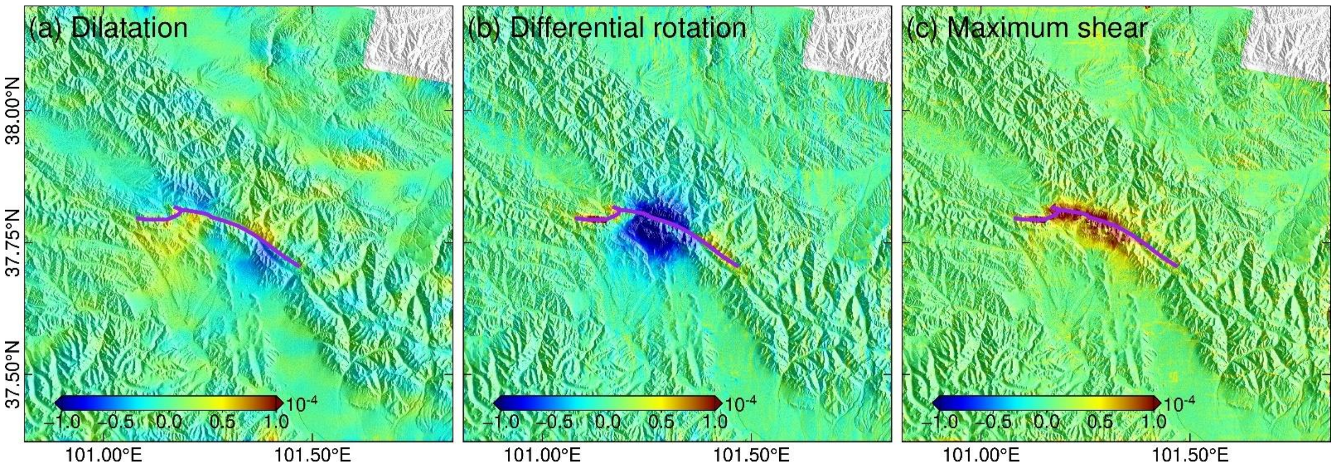

Figure 5. Three strain invariants for the 2022 Menyuan earthquake. Note that the strain invariants are dimensionless (i.e., no unit). (**a**–**c**) are dilatation, differential rotation, and maximum shear maps, respectively.

For the 2022 Menyuan earthquake, it was easy to obtain the SAR displacement observations along two geometries, i.e., ascending and descending LOS direction, using only on the free Sentinel-1 SAR data (e.g., Figure 2e,i). Due to the low azimuth pixel's spatial resolution of Sentinel-1 SAR images, the signal-to-noise ratio (SNR) of the POT-derived azimuth displacement observations (e.g., Figure 2g,k) was too low to identify any valuable displacement signal. Although the displacement accuracy was relatively high for the BOI observations compared with the POT azimuth observations, the BOI coverage was too limited to reveal the detailed spatial variety of surface displacements. In this case, if considering only the free Sentinel-1 SAR data, one can hardly obtain complete and accurate 3D displacements associated with this event. Unlike the Sentinel-1 SAR images, the azimuth pixel's spatial resolution of the ALOS-2 SAR images is as high as 2–3 m; therefore, the POT method is sufficient to measure the azimuth displacement with considerable accuracy. Simultaneously, the MAI method can also be applied to the ALOS-2 SAR data to derive the azimuth displacement observation, which shares the same imaging geometry with the POT azimuth displacement observation. In this sense, the ALOS-2 azimuth displacement observations (e.g., Figure 2o,p) play a very important role in calculating the 3D displacements of this event, especially by contributing to the north–south displacement component, since other SAR displacement observations in Figure 2 cannot adequately reveal the displacement pattern in the satellite azimuth geometry.

4.3. Calculating the Displacements/Strains near the Ruptured Fault Zone

When calculating the displacements or strains of a target point, it is inevitable to incorporate the surrounding points. For example, when calculating the 3D displacements using the SM-VCE method, one should establish the observation functions (i.e., Equation (11)) on the basis of the observations within a predefined window. When calculating the strain invariants, it is also necessary to use the 3D displacements at surrounding points. One should pay attention that the precondition for reliable calculation of the displacements/strains lies such that the displacement gradients among these surrounding points are constant. However, when the target point is located near the ruptured fault and these surrounding points are located on both sides of the fault, it is obvious that the displacement gradients are different among these points. In this case, if the surrounding points on the other side of the fault are not distinguished and not discarded in the calculation, the obtained displacements/strains will be contaminated and cannot appropriately reflect the real deformation pattern.

For the 2022 Menyuan earthquake, the fault ruptured the ground surface, and there were displacement jumps across the ruptured fault. In order to accurate calculate the displacements/strains near the ruptured fault zone, we first manually mapped the fault traces on the basis of POT observations and excluded those points on the opposite side of the fault in the calculation. One can image that if those points on the opposite side of the fault were not excluded, the obtained 3D displacements would be very smooth across the fault. Moreover, since the strain invariants were calculated on the basis of the displacement gradients, the magnitude of the strain invariants would be very large near the displacement jump zone compared with the far-field zone. These possible results are wrong and do not correspond with the real deformation of earthquakes.

5. Conclusions

This paper calculated the 3D surface displacements of the 2022 Menyuan earthquake using ascending/descending Sentinel-1 SAR data and descending ALOS-2 SAR data. To derive SAR displacement observations along different directions (i.e., the satellite line-of-sight and azimuth directions), DInSAR, POT, MAI, and/or BOI methods were applied to process these SAR data. With such abundant SAR displacement observations from various observing directions, it is clear that the co-seismic deformation of this earthquake could be well constrained. Afterward, an SM-VCE method was used to combine these SAR displacement observations to obtain a high-accuracy 3D displacement field. Since the SM was used to establish the relationship between SAR observations and 3D displacements, and since the VCE was used to determine the accurate weights of SAR observations in the SM-VCE method, the obtained 3D co-seismic displacement was more accurate and reliable compared with the traditional WLS method, and the precision was generally at the level of centimeters to millimeters in this study. Results indicate that the 2022 Menyuan earthquake was dominated by left-lateral slip, and the maximum horizontal and vertical displacements were ~1.9 m and 0.6 m, respectively. The relative horizontal surface displacement across the fault was as large as 2–3 m, and the fault-parallel displacement magnitude was larger on the southern side of the fault compared with the northern side. Furthermore, three strain invariants were also calculated and revealed that the near-fault zones suffered the most severe strains, and two expanding and compressed zones were also identified.

To calculate reliable 3D displacements near the fault zone, the manually mapped fault traces from the SAR POT observations were used to assist the SM-VCE method. However, the manually mapped fault traces are not always available; thus, it is necessary to apply some automatic algorithms to increase the robustness of SM-VCE method near the displacement jump zone. Additionally, since the SM-VCE method uses more observations to calculate 3D displacements, the computational efficiency still has much room for improvement. Given that this study aimed to provide a quick and reliable 3D displacement field of the 2022 Menyuan earthquake, we did not investigate the fault model of this event. Although some fault models have been published on the basis of DInSAR LOS observations (e.g., [2,11]) or seismic wave data (e.g., [1,51]), it is worthy to conduct a slip model inversion using the obtained 3D displacements in the future.

Author Contributions: Conceptualization, J.L. and J.H.; methodology, J.L. and J.S.; software, J.L.; validation, J.L. and Z.M.; formal analysis, J.L. and Z.M.; investigation, J.S.; resources, Z.L. and W.X.; writing—original draft preparation, J.L., Z.M. and J.S.; writing—review and editing, J.H., Z.M. and Q.S.; visualization, J.L. and J.S.; supervision, J.H. and Q.S.; project administration, J.L.; funding acquisition, J.H. All authors have read and agreed to the published version of the manuscript.

Funding: This research was funded by the National Key Basic Research and Development Program of China (grant number 2018YFC1503603), the National Natural Science Foundation of China (grant number 42030112), the Nature Science Foundation of Hunan Province (grant number 2020JJ2043), the Project of Innovation-Driven Plan of Central South University (grant number 2019CX007), the Fundamental Research Funds for the Central Universities of Central South University (grant numbers 2018zzts684 and 2019zzts011), and the Hunan Provincial Innovation Foundation For Postgraduate (grant number CX20190067).

Institutional Review Board Statement: Not applicable.

Informed Consent Statement: Not applicable.

Data Availability Statement: The displacement data presented in this study are openly available from Zenodo at https://doi.org/10.5281/zenodo.6018283 (8 March 2022), and an SM-VCE code demo for calculating 3D co-seismic displacements of the 8 January 2022 Mw6.7 Menyuan earthquake is openly available from Zenodo at https://doi.org/10.5281/zenodo.6326993 (8 March 2022).

Acknowledgments: The ALOS-2 data were provided by the Japan Aerospace Exploration Agency (JAXA), and the Sentinel-1 data were provided by ESA/Copernicus (https://scihub.copernicus.eu/) (8 March 2022). We thank the editors and three anonymous reviewers for their constructive comments and suggestions.

Conflicts of Interest: The authors declare no conflict of interest.

References

1. Xu, Y.; Guo, X.; Feng, L. Relocation and focal mechanism solutions of the Ms6.9 Menyuan earthquake sequence on January 8, 2022 in Qinghai Province. *Acta Seismol. Sin.* **2022**, *44*, 1–16. [CrossRef]
2. Li, Z.; Han, B.; Liu, Z.; Zhang, M.; Yu, C.; Chen, B.; Liu, H.; Du, J.; Zhang, S.; Zhu, W.; et al. Source Parameters and Slip Distributions of the 2016 and 2022 Menyuan, Qinghai Earthquakes Constrained by InSAR Observations. *Geomat. Inf. Sci. Wuhan Univ.* **2022**. [CrossRef]
3. Zheng, W.-J.; Zhang, P.-Z.; He, W.-G.; Yuan, D.-Y.; Shao, Y.-X.; Zheng, D.-W.; Ge, W.-P.; Min, W. Transformation of displacement between strike-slip and crustal shortening in the northern margin of the Tibetan Plateau: Evidence from decadal GPS measurements and late Quaternary slip rates on faults. *Tectonophysics* **2013**, *584*, 267–280. [CrossRef]
4. Guo, P.; Han, Z.; An, Y.; Jiang, W.; Mao, Z.; Feng, W. Activity of the Lenglongling fault system and seismotectonics of the 2016 M_S6.4 Menyuan earthquake. *Sci. China Earth Sci.* **2017**, *60*, 929–942. [CrossRef]
5. Jiang, W.-L.; Li, Y.-S.; Tian, Y.-F.; Han, Z.-J.; Zhang, J.-F. Research of seismogenic structure of the Menyuan M_S6.4 earthquake on January 21, 2016 in Lenglongling area of NE Tibetan plateau. *Seismol. Egology* **2017**, *39*, 536. [CrossRef]
6. Qu, W.; Gao, Y.; Chen, H.-L.; Liang, S.-C.; Han, Y.-X.; Zhang, Q.; Wang, Q.-L.; Hao, M. Review on Characteristics of Present Crustal Tectonic Movement and Deformation in Qinghai-Tibet Plateau, China Using GPS High Precision Monitoring Data. *J. Earth Sci. Environ.* **2021**, *43*, 182–204. [CrossRef]
7. Hao, M.; Li, Y.; Zhuang, W. Crustal movement and strain distribution in East Asia revealed by GPS observations. *Sci. Rep.* **2019**, *9*, 16797. [CrossRef] [PubMed]
8. Gaudemer, Y.; Tapponnier, P.; Meyer, B.; Peltzer, G.; Shunmin, G.; Zhitai, C.; Huagung, D.; Cifuentes, I. Partitioning of crustal slip between linked, active faults in the eastern Qilian Shan, and evidence for a major seismic gap, the 'Tianzhu gap', on the western Haiyuan Fault, Gansu (China). *Geophys. J. Int.* **1995**, *120*, 599–645. [CrossRef]
9. Lasserre, C.; Gaudemer, Y.; Tapponnier, P.; Mériaux, A.S.; Van der Woerd, J.; Daoyang, Y.; Ryerson, F.; Finkel, R.; Caffee, M. Fast late Pleistocene slip rate on the Leng Long Ling segment of the Haiyuan fault, Qinghai, China. *J. Geophys. Res. Solid Earth* **2002**, *107*, ETG 4-1–ETG 4-15. [CrossRef]
10. Li, Y.; Gan, W.; Wang, Y.; Chen, W.; Zhang, K.; Liang, S.; Zhang, Y. Seismogenic Structure of the 2016 Ms6.4 Menyuan Earthquake and its Effect on the Tianzhu Seismic Gap. *J. Geod. Geodyn.* **2017**, *37*, 792. [CrossRef]
11. Yang, H.; Wang, D.; Guo, R.; Xie, M.; Zang, Y.; Wang, Y.; Yao, Q.; Cheng, C.; An, Y.; Zhang, Y. Rapid report of the 8 January 2022 Ms 6.9 Menyuan earthquake, Qinghai, China. *Earthq. Res. Adv.* **2022**, 100113. [CrossRef]
12. Gabriel, A.K.; Goldstein, R.M.; Zebker, H.A. Mapping small elevation changes over large areas: Differential radar interferometry. *J. Geophys. Res. Solid Earth* **1989**, *94*, 9183–9191. [CrossRef]
13. Michel, R.; Avouac, J.P.; Taboury, J. Measuring ground displacements from SAR amplitude images: Application to the Landers Earthquake. *Geophys. Res. Lett.* **1999**, *26*, 875–878. [CrossRef]

14. Bechor, N.B.D.; Zebker, H.A. Measuring two-dimensional movements using a single InSAR pair. *Geophys. Res. Lett.* **2006**, *33*, 275–303. [CrossRef]
15. Grandin, R.; Klein, E.; Métois, M.; Vigny, C. 3D displacement field of the 2015 M_W8.3 Illapel earthquake (Chile) from across- and along-track Sentinel-1 TOPS interferometry. *Geophys. Res. Lett.* **2016**, *43*, 2552–2561. [CrossRef]
16. Jung, H.S.; Lu, Z.; Won, J.S.; Poland, M.P.; Miklius, A. Mapping Three-Dimensional Surface Deformation by Combining Multiple-Aperture Interferometry and Conventional Interferometry: Application to the June 2007 Eruption of Kilauea Volcano, Hawaii. *IEEE Geosci. Remote Sens. Lett.* **2011**, *8*, 34–38. [CrossRef]
17. Wright, T.J.; Parsons, B.E.; Lu, Z. Toward mapping surface deformation in three dimensions using InSAR. *Geophys. Res. Lett.* **2004**, *31*, 169–178. [CrossRef]
18. Liu, J.; Hu, J.; Li, Z.; Zhu, J.J.; Sun, Q.; Gan, J. A Method for Measuring 3-D Surface Deformations With InSAR Based on Strain Model and Variance Component Estimation. *IEEE Trans. Geosci. Remote Sens.* **2018**, *56*, 239–250. [CrossRef]
19. Liu, J.; Hu, J.; Xu, W.; Li, Z.; Zhu, J.; Ding, X.; Zhang, L. Complete three-dimensional co-seismic deformation fields of the 2016 Central Tottori earthquake by integrating left- and right-looking InSAR with the improved SM-VCE method. *J. Geophys. Res. Solid Earth* **2019**, *124*, 12099–12115. [CrossRef]
20. Hu, J.; Liu, J.; Li, Z.; Zhu, J.; Wu, L.; Sun, Q.; Wu, W. Estimating three-dimensional coseismic deformations with the SM-VCE method based on heterogeneous SAR observations: Selection of homogeneous points and analysis of observation combinations. *Remote Sens. Environ.* **2021**, *255*, 112298. [CrossRef]
21. Liu, J.; Hu, J.; Li, Z.; Ma, Z.; Wu, L.; Jiang, W.; Feng, G.; Zhu, J. Complete three-dimensional coseismic displacements due to the 2021 Maduo earthquake in Qinghai Province, China from Sentinel-1 and ALOS-2 SAR images. *Sci. China Earth Sci.* **2022**, *65*, 1–11. [CrossRef]
22. Fialko, Y. Evidence of fluid-filled upper crust from observations of postseismic deformation due to the 1992 M_W7.3 Landers earthquake. *J. Geophys. Res. Solid Earth* **2004**, *109*. [CrossRef]
23. Jacobs, A.; Sandwell, D.; Fialko, Y.; Sichoix, L. The 1999 (M_W7.1) Hector Mine, California, earthquake: Near-field postseismic deformation from ERS interferometry. *Bull. Seismol. Soc. Am.* **2002**, *92*, 1433–1442. [CrossRef]
24. Hu, J.; Li, Z.; Zhu, J.; Zhang, L.; Sun, Q. 3D coseismic Displacement of 2010 Darfield, New Zealand earthquake estimated from multi-aperture InSAR and D-InSAR measurements. *J. Geod.* **2012**, *86*, 1029–1041. [CrossRef]
25. Vaníček, P.; Grafarend, E.W.; Berber, M. Short Note: Strain invariants. *J. Geod.* **2008**, *82*, 263–268. [CrossRef]
26. Guglielmino, F.; Nunnari, G.; Puglisi, G.; Spata, A. Simultaneous and Integrated Strain Tensor Estimation From Geodetic and Satellite Deformation Measurements to Obtain Three-Dimensional Displacement Maps. *IEEE Trans. Geosci. Remote Sens.* **2011**, *49*, 1815–1826. [CrossRef]
27. Hu, J.; Li, Z.; Sun, Q.; Zhu, J.J.; Ding, X.L. Three-Dimensional Surface Displacements From InSAR and GPS Measurements With Variance Component Estimation. *IEEE Geosci. Remote Sens. Lett.* **2012**, *9*, 754–758. [CrossRef]
28. Hu, S.W.; Xiao, B.L. *Modern Theory and Application of Surveying Data Processing*; Surveying and Mapping Press: Beijing, China, 2016. (In Chinese)
29. Yuan, D.; Zhang, P.; Liu, B.; Gan, W.; Mao, F.; Wang, Z.; Zheng, W.; Guo, H. Geometrical Imagery and Tectonic Transformation of Late Quaternary Active Tectonics in Northeastern Margin of Qinghai-Xizang Platean. *Acta Geol. Sin.* **2004**, *78*, 270. (In Chinese)
30. Liu, J.; Hu, J.; Li, Z.; Sun, Q.; Ma, Z.; Zhu, J.; Wen, Y. Dynamic Estimation of Multi-Dimensional Deformation Time Series from InSAR Based on Kalman Filter and Strain Model. *IEEE Trans. Geosci. Remote Sens.* **2022**, *60*. [CrossRef]
31. Clarke, P.J.; Davies, R.R.; England, P.C.; Parsons, B.; Billiris, H.; Paradissis, D.; Veis, G.; Cross, P.A.; Denys, P.H.; Ashkenazi, V.; et al. Crustal strain in central Greece from repeated GPS measurements in the interval 1989–1997. *Geophys. J. Int.* **1998**, *135*, 195–214. [CrossRef]
32. Lin, K.C.; Hu, J.C.; Ching, K.E.; Angelier, J.; Rau, R.J.; Yu, S.B.; Tsai, C.H.; Shin, T.C.; Huang, M.H. GPS crustal deformation, strain rate and seismic activity after the 1999 Chi-Chi earthquake in Taiwan. *J. Geophys. Res. Solid Earth* **2010**, *115*, 1–22. [CrossRef]
33. Shen, Z.-K.; Jackson, D.D.; Ge, B.X. Crustal deformation across and beyond the Los Angeles basin from geodetic measurements. *J. Geophys. Res. Solid Earth* **1996**, *101*, 27957–27980. [CrossRef]
34. Mehrabi, H. Three-dimensional strain descriptors at the Earth's surface through 3D retrieved co-event displacement fields of differential interferometric synthetic aperture radar. *J. Geod.* **2021**, *95*, 39. [CrossRef]
35. Hu, J.; Wang, Q.J.; Li, Z.W.; Xie, R.A.; Zhang, X.Q.; Sun, Q. Retrieving three-dimensional coseismic displacements of the 2008 Gaize, Tibet earthquake from multi-path interferometric phase analysis. *Nat. Hazards* **2014**, *73*, 1311–1322. [CrossRef]
36. Gan, J.; Hu, J.; Li, Z.; Yang, C.; Liu, J.; Sun, Q.; Zheng, W. Mapping three-dimensional co-seismic surface deformations associated with the 2015 Mw7.2 Murghab earthquake based on InSAR and characteristics of crustal strain. *Sci. China Earth Sci.* **2018**, *61*, 1451–1466. [CrossRef]
37. Zhao, D.; Qu, C.; Chen, H.; Shan, X.; Song, X.; Gong, W. Tectonic and Geometric Control on Fault Kinematics of the 2021 Mw7. 3 Maduo (China) Earthquake Inferred From Interseismic, Coseismic, and Postseismic InSAR Observations. *Geophys. Res. Lett.* **2021**, *48*, e2021GL095417. [CrossRef]
38. Samsonov, S.; D'Oreye, N. Multidimensional time-series analysis of ground deformation from multiple InSAR data sets applied to Virunga Volcanic Province. *Geophys. J. Int.* **2012**, *191*, 1095–1108. [CrossRef]
39. Hu, J.; Ding, X.L.; Li, Z.W.; Zhu, J.J.; Sun, Q.; Zhang, L. Kalman-Filter-Based Approach for Multisensor, Multitrack, and Multitemporal InSAR. *IEEE Trans. Geosci. Remote Sens.* **2013**, *51*, 4226–4239. [CrossRef]

40. Liu, J.; Hu, J.; Burgmann, R.; Li, Z.; Sun, Q.; Ma, Z. A Strain-Model Based InSAR Time Series Method and its Application to The Geysers Geothermal Field, California. *J. Geophys. Res. Solid Earth* **2021**, *126*, e2021JB021939. [CrossRef]
41. Pepe, A.; Solaro, G.; Calo, F.; Dema, C. A Minimum Acceleration Approach for the Retrieval of Multiplatform InSAR Deformation Time Series. *IEEE J. Sel. Top. Appl. Earth Obs. Remote Sens.* **2016**, *9*, 3883–3898. [CrossRef]
42. Samsonov, S.; D'Oreye, N. Multidimensional Small Baseline Subset (MSBAS) for Two-Dimensional Deformation Analysis: Case Study Mexico City. *J. Geod.* **2017**, *43*, 318–329. [CrossRef]
43. Morishita, Y.; Kobayashi, T.; Yarai, H. Three-dimensional deformation mapping of a dike intrusion event in Sakurajima in 2015 by exploiting the right- and left-looking ALOS-2 InSAR. *Geophys. Res. Lett.* **2016**, *43*, 4197–4204. [CrossRef]
44. Fialko, Y.; Sandwell, D.; Simons, M.; Rosen, P. Three-dimensional deformation caused by the Bam, Iran, earthquake and the origin of shallow slip deficit. *Nature* **2005**, *435*, 295–299. [CrossRef]
45. Funning, G.J.; Parsons, B.; Wright, T.J.; Jackson, J.A.; Fielding, E.J. Surface displacements and source parameters of the 2003 Bam (Iran) earthquake from Envisat advanced synthetic aperture radar imagery. *J. Geophys. Res. Solid Earth* **2005**, *110*. [CrossRef]
46. Jo, M.J.; Jung, H.S.; Won, J.S. Measurement of precise three-dimensional volcanic deformations via TerraSAR-X synthetic aperture radar interferometry. *Remote Sens. Environ.* **2017**, *192*, 228–237. [CrossRef]
47. Jo, M.J.; Jung, H.S.; Won, J.S.; Poland, M.P.; Miklius, A.; Lu, Z. Measurement of slow-moving along-track displacement from an efficient multiple-aperture SAR interferometry (MAI) stacking. *J. Geod.* **2015**, *89*, 411–425. [CrossRef]
48. He, P.; Wen, Y.; Xu, C.; Chen, Y. High-quality three-dimensional displacement fields from new-generation SAR imagery: Application to the 2017 Ezgeleh, Iran, earthquake. *J. Geod.* **2018**, *93*, 573–591. [CrossRef]
49. He, P.; Wen, Y.; Xu, C.; Chen, Y. Complete three-dimensional near-field surface displacements from imaging geodesy techniques applied to the 2016 Kumamoto earthquake. *Remote Sens. Environ.* **2019**, *232*, 111321. [CrossRef]
50. Wang, X.; Liu, G.; Yu, B.; Dai, K.; Zhang, R.; Ma, D.; Li, Z. An integrated method based on DInSAR, MAI and displacement gradient tensor for mapping the 3D coseismic deformation field related to the 2011 Tarlay earthquake (Myanmar). *Remote Sens. Environ.* **2015**, *170*, 388–404. [CrossRef]
51. Han, L. Focal mechanism of 2022 Menyuan MS6.9 earthquake in Qinghai Province. *Prog. Earthq. Sci.* **2022**, *52*, 49–54. [CrossRef]